# Solution Structure of Ln(III) Complexes with Macrocyclic Ligands Through Theoretical Evaluation of ¹H NMR Contact Shifts

Aurora Rodríguez-Rodríguez,[†] David Esteban-Gómez,[†] Andrés de Blas,[†] Teresa Rodríguez-Blas,[†] Mauro Botta,[‡] Raphaël Tripier,[§] and Carlos Platas-Iglesias*[,†]

[†]Departamento de Química Fundamental, Facultade de Ciencias, Universidade da Coruña, Campus da Zapateira-Rúa da Fraga 10, 15008 A Coruña, Spain.

[‡]Dipartimento di Scienze e Innovazione Tecnologica, Università del Piemonte Orientale "Amedeo Avogadro", Viale T. Michel 11, 15121 Alessandria, Italy

[§]Université de Bretagne Occidentale, UMR-CNRS 6521, UFR des Sciences et Techniques, 6 avenue Victor le Gorgeu, C.S. 93837, 29238 BREST Cedex 3, France

**S** *Supporting Information*

**ABSTRACT:** Herein, we present a new approach that combines DFT calculations and the analysis of Tb^{III}-induced ¹H NMR shifts to quantitatively and accurately account for the contact contribution to the paramagnetic shift in Ln^{III} complexes. Geometry optimizations of different Gd^{III} complexes with macrocyclic ligands were carried out using the hybrid meta-GGA TPSSh functional and a $46 + 4f^7$ effective core potential (ECP) for Gd. The complexes investigated include [Ln(Me-DODPA)]^+ (H_2Me-DODPA = 6,6′-((4,10-dimethyl-1,4,7,10-tetraazacyclododecane-1,7-diyl)bis-(methylene))dipicolinic acid, [Ln(DOTA)(H_2O)]^−



(H_4DOTA = 1,4,7,10-tetraazacyclododecane-1,4,7,10-tetraacetate), [Ln(DOTAM)(H_2O)]^{3+} (DOTAM = 1,4,7,10- tetrakis[(carbamoyl)methyl]-1,4,7,10-tetraazacyclododecane), and related systems containing pyridyl units (Ln = Gd, Tb). Subsequent all-electron relativistic calculations based on the DKH2 approximation, or small-core ECP calculations, were used to compute the ¹H hyperfine coupling constants (HFCCs) at the ligand nuclei ($A_{iso}$ values). The calculated $A_{iso}$ values provided direct access to contact contributions to the ¹H NMR shifts of the corresponding Tb^{III} complexes under the assumption that Gd and Tb complexes with a given ligand present similar HFCCs. These contact shifts were used to obtain the pseudocontact shifts, which encode structural information as they depend on the position of the nucleus with respect to the lanthanide ion. An excellent agreement was observed between the experimental and calculated pseudocontact shifts using the DFT-optimized geometries as structural models of the complexes in solution, which demonstrates that the computational approach used provides (i) good structural models for the complexes, (ii) accurate HFCCs at the ligand nuclei. The methodology presented in this work can be classified in the context of model-dependent methods, as it relies on the use of a specific molecular structure obtained from DFT calculations. Our results show that spin polarization effects dominate the ¹H $A_{iso}$ values. The X-ray crystal structures of [Ln(Me-DODPA)](PF_6)·2H_2O (Ln = Eu or Lu) are also reported.
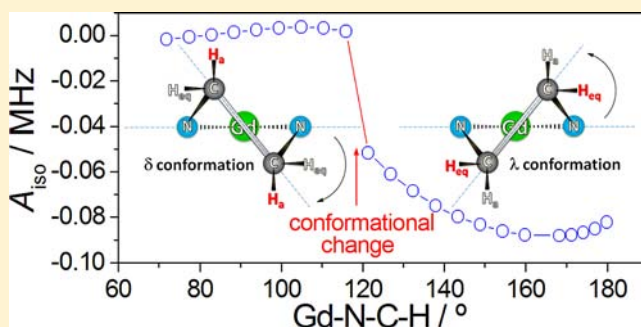
## ■ INTRODUCTION

Stable lanthanide(III) complexes with macrocyclic ligands have attracted considerable attention during the last two decades due to their application as contrast agents (CAs) in magnetic resonance imaging,[1,2] radiopharmaceuticals for imaging and therapy,[3] and luminescence probes in biomedical analyses and imaging.[4] Additionally, paramagnetic lanthanide(III) ions and complexes have been widely used as NMR shift reagents,[5] paramagnetic probes for structure determination of biomolecules,[6] and mapping protein surface accessibility.[7] Recently, negatively charged paramagnetic Ln^{III} complexes have been also proposed as NMR probes to explore regions with positive electrostatic potential on the surface of positively charged species.[8] In spite of the very successful application of different

Ln^{III} complexes in these fields, a rational design of Ln^{III} complexes with improved properties requires a detailed understanding of their structure in solution.

The interpretation of NMR spectra of paramagnetic Ln^{III} complexes is not as straightforward as that for the diamagnetic analogues of La^{III} or Lu^{III}.[9−12] The main reason is that paramagnetic shifts are related to the unpaired spin density, and both contact and pseudocontact mechanisms might provide sizable contributions to the overall paramagnetic shifts in small Ln^{III} complexes. Thus, theoretical calculations of paramagnetic shifts are important to gain a better understanding of how

structure and chemical bonding determine the observed paramagnetic shifts. Besides, an inspection of the expressions accounting for the contact and pseudocontact contributions (below) shows that only the pseudocontact term provides quantitative information on the structure of the Ln[III] complexes in solution. Theoretical evaluation of contact shifts can therefore provide direct access to the pseudocontact contributions and thus to information on the structure of a given complex in solution.

Different methods were proposed, and successfully applied, for the separation of contact and dipolar contributions in Ln[III] complexes.[13] These methods generally require to assume that: (i) a given series of Ln[III] complexes are isostructural along the lanthanide series; (ii) the pseudocontact shifts are proportional to the Bleaney constants, which are characteristic of the particular Ln[III] ion, and were calculated with the assumption that the ligand field splittings for the lowest $J$ state are small compared to $kT$;[14] (iii) the hyperfine coupling constants do not change substantially along the lanthanide series. Alternatively, the hyperfine ^{1}H NMR shifts in Yb[III] complexes can be directly analyzed assuming that they are mainly pseudocontact in origin,[15,16] as the theoretical value for the ratio of the contact to pseudocontact contribution is as low as 0.12.[17] In spite of the very successful application of Ln[III]-induced paramagnetic shifts to obtain information on the solution structure of many lanthanide complexes,[9−12] little progress has been done on the theoretical calculation of paramagnetic shifts of these systems. In recent articles, Autschbach et al.[18,19] calculated the pseudocontact shifts in $[Ce(DPA)_3]^{3-}$ ($H_2DPA$ = dipicolinic acid) and different Ru(III) complexes by using the zeroth-order regular approximation and DFT.

The contact contribution to the paramagnetic shift is related to the isotropic hyperfine coupling constant, which depends upon the spin density at the position of the observed nucleus, and therefore can be calculated with the aid of DFT calculations. Indeed, different computational studies have shown that ^{1}H hyperfine coupling constants in organic radicals[20] and transition metal complexes[21] can be accurately calculated with the use of DFT. Recently, we have also reported a simple computational recipe based on DFT for the theoretical calculations of [17]O hyperfine coupling constants of coordinated water molecules in Gd[III] complexes.[22] An accurate theoretical calculation of [1]H $A_{iso}$ values obviously provides a direct access to the contact contributions in Ln[III] complexes, and therefore to the pseudocontact shifts as well, thereby allowing a straightforward analysis of the structure in solution of Ln[III] complexes. Among the different Ln[III] ions, Gd[III] is an obvious candidate for such calculations, as its symmetric electronic ground state ($^8S$) avoids the largely unresolved theoretical issue of spin−orbit coupling in other open-shell Ln[III] complexes. It must be pointed out that for a f[7] ion such as Gd[III], the ligand field splitting is zero under first order conditions, and therefore no pseudocontact contribution to the paramagnetic shifts is expected. For all other paramagnetic Ln[III] complexes both contact and pseudocontact contributions are expected to operate.

In a recent article, we have reported a series of Ln[III] complexes with the macrocyclic ligand Me-DODPA[2−] (Chart 1),[23] which has been designed for stable lanthanide complexation in aqueous solution. The solution structure of these complexes was investigated by analyzing the Yb[III]-induced ^{1}H NMR shifts. Herein, we report the X-ray structures of the Eu[III] and Lu[III] complexes with this ligand, as well as a detailed

**Chart 1. Ligands Discussed in the Present Work with the Numbering Schemes Used for NMR Spectral Assignment**
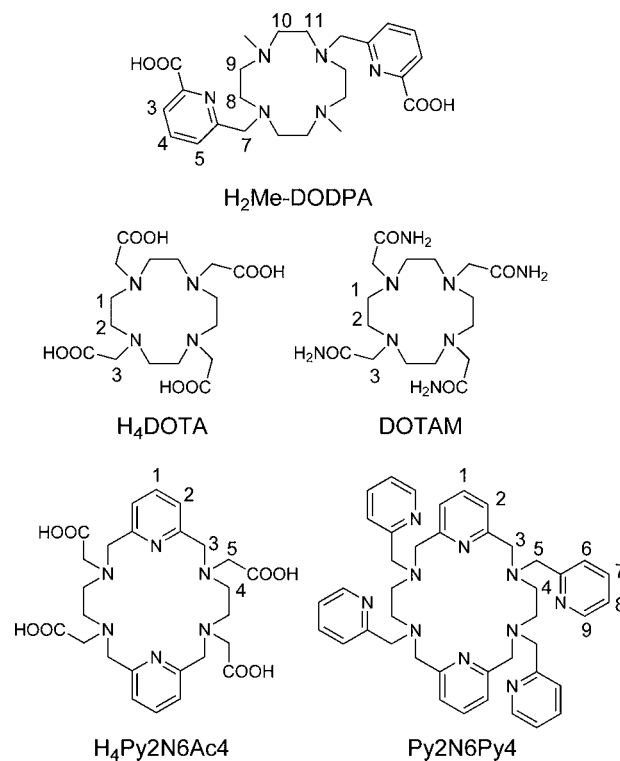


analysis of the Tb[III]-induced ^{1}H NMR shifts. DFT calculations were used to obtain ^{1}H hyperfine coupling constants for the $[Gd(Me\text{-}DODPA)]^+$ complex. Tb is next to Gd in the periodic table, and therefore Tb[III] and Gd[III] have nearly the same ratio of charge to ionic radius and correspondingly similar coordination chemistry. Furthermore, it has been shown that $A/\hbar$ is constant along different series of isostructural lanthanide complexes.[9,12] Thus, the isotropic HFCCs are expected to be very similar for isoestructural Gd[III] and Tb[III] complexes, which allows to estimate the contact shifts of Tb[III] complexes from the ^{1}H hyperfine coupling constants calculated for the Gd[III] analogues.[9] Subtraction of these contact shifts from the observed paramagnetic shifts for the Tb[III] complex provided the corresponding pseudocontact shifts. This semiempirical approach avoids the difficult part of using Ln[III] complexes other than Gd[III] for theoretical evaluation of paramagnetic shifts. However, a good agreement between these pseudocontact shifts and those calculated with the DFT optimized structures would prove the accuracy of both the calculated contact shifts and the structures of the complexes obtained from DFT calculations.

The methodology developed for $[Ln(Me\text{-}DODPA)]^+$ complexes has been also applied to $[Gd(DOTA)(H_2O)]^-$, which is currently applied as a contrast agent in MRI under the name Dotarem (gadoterate meglumine, Guerbet, Aulnaysous-Bois, France), and $[Gd(DOTAM)]^{3+}$, a representative compound of a second class of paramagnetic lanthanide(III)-based contrast agents that take advantage of the chemical exchange saturation transfer (CEST) mechanism.[11] In spite of the enormous interest of Ln[III] complexes, mostly due to their applications in MRI, it is hard to find ^{1}H NMR spectral data for Tb[III] complexes. Among the well-characterized Tb[III] complexes whose ^{1}H NMR spectra have been reported are [Tb-

$(Py2N4Ac4)]^-$ and $[Tb(Py2N4Py4)]^{3+}$ complexes, which present a $D_2$ symmetry in aqueous solution.[24,25] Thus, the solution structure of these complexes has been also investigated by theoretical evaluation of the $^1H$ NMR shifts in the $Gd^{III}$ analogues and subsequent analysis of the $Tb^{III}$-induced pseudocontact shifts. We must note that the procedure presented here falls into the category of the model-dependent methods, as it relies on the assumption of a particular geometry of the complex in solution.[12a]

## LN$^{III}$-INDUCED PARAMAGNETIC SHIFTS

The binding of a ligand to a paramagnetic $Ln^{III}$ ion results in large frequency shifts of the NMR signals due to ligand nuclei, with magnitudes and signs depending on both the location of the nucleus relative to the metal center and the nature of the lanthanide ion. Thus, the analysis of $Ln^{III}$-induced paramagnetic shifts has been widely used to investigate the structure of the corresponding complexes in solution.[9−12] For a given nucleus $i$, the isotropic paramagnetic shift induced by a lanthanide ion $j$ $(\delta_{ij}^{para})$ may be written as a combination of the Fermi contact $(\delta_{ij}^{con})$ and pseudocontact $(\delta_{ij}^{pscon})$ contributions:

$$\delta_{ij}^{para} = \delta_{ij}^{exp} - \delta_i^{dia} = \delta_{ij}^{con} + \delta_{ij}^{pscon} \tag{1}$$

where $\delta_{ij}^{exp}$ represents the experimentally observed chemical shift and $\delta_i^{dia}$ denotes the diamagnetic contribution, which can be estimated by measuring the chemical shifts for analogous diamagnetic complexes ($La^{III}$, $Lu^{III}$, or $Y^{III}$). Contact shifts arise from through-bond transmission of unpaired electron-spin density from the $Ln^{III}$ ion to the nucleus under study, and they can be expressed as in eq 2:[9]

$$\delta_{ij}^{con} = \langle S_z \rangle_j \frac{\mu_B}{3kT\gamma_I} \frac{A}{\hbar} 10^6 \tag{2}$$

where $\langle S_z \rangle$ is the reduced value of the average spin polarization, $\mu_B$ is the Bohr magneton, $k$ the Boltzmann constant, $\gamma_I$ the gyromagnetic ratio of the observed nucleus, $A/\hbar$ the hyperfine coupling constant (HFCC, in rad·s$^{-1}$), and $\delta_{ij}^{con}$ is expressed in ppm.

The pseudocontact contribution results from the local magnetic field induced in the nucleus under study by the magnetic moment of the $Ln^{III}$ ion, and can be written as linear combinations of the five components of the magnetic susceptibility tensor $\chi$ as given by the following equation:[26]

$$\delta_{ij}^{pscon} = \left(\chi_{zz} - \frac{1}{3}Tr\chi\right)\left(\frac{3z^2 - r^2}{r^5}\right) + (\chi_{xx} - \chi_{yy})$$
$$\left(\frac{x^2 - y^2}{r^5}\right) + \chi_{xy}\left(\frac{4xy}{r^5}\right) + \chi_{xz}\left(\frac{4xz}{r^5}\right) + \chi_{yz}\left(\frac{4yz}{r^5}\right) \tag{3}$$

where $r = (x^2 + y^2 + z^2)^{1/2}$ and $x$, $y$, and $z$ are the Cartesian coordinates of a nucleus $i$ relative to the location of a $Ln^{III}$ ion $j$. In the principal magnetic axis system, the last three terms of eq 3 vanish, as $\chi_{xy} = \chi_{xz} = \chi_{yz} = 0$. For the special case of axial symmetry, that is, systems containing a $C_n$ axis with $n \geq 3$, $\chi_{xx} - \chi_{yy} = 0$, and therefore only the first term of eq 3 remains.

The isotropic HFCC ($A_{iso}$) for the nucleus $N$ is determined by the Fermi contact interaction (eq 4), and provides a direct measure of the net spin density at the various nuclei of a given molecule.[27]

$$A_{iso}(N) = \frac{4\pi}{3S}\beta_e\beta_N g_e g_N \rho^{\alpha-\beta}(R_N) \tag{4}$$

where $\beta_N$ and $\beta_e$ are the nuclear and Bohr magnetons, respectively, $g_N$ and $g_e$ are nuclear and free-electron g values, $S$ is the total electron spin of the system, and $\rho^{\alpha-\beta}(R_N)$ represents the difference between majority spin ($\alpha$) and minority spin ($\beta$) densities at the position of the nucleus $N$, and $A_{iso}$ equals $A/\hbar/2\pi$ as defined in eq 2. Thus, $A_{iso}$ is proportional to the value of the spin density at the position of nucleus $N$.

## ■ EXPERIMENTAL AND COMPUTATIONAL METHODS

**Single-Crystal X-ray Crystallography.** 3D X-ray data were collected on a Bruker X8 APEXII CCD diffractometer. Data were corrected for Lorentz and polarization effects and for absorption by semiempirical methods[28] based on symmetry-equivalent reflections. Complex scattering factors were taken from the program *SHELX97*[29] running under the *WinGX* program system[30] as implemented on a Pentium computer. Both structures were solved by Patterson methods (DIRDIF2008[31]) and refined[29] by full-matrix least-squares on $F^2$. All hydrogen atoms were included in calculated positions and refined in riding mode in both compounds, except those of water molecules that were located in a difference electron-density map and refined freely. Refinement converged with anisotropic displacement parameters for all non-hydrogen atoms. Crystal data and details on data collection and refinement are summarized in Table 1.

**Table 1. Crystal Data and Refinement Details for [Ln(Me-DODPA)](PF$_6$)·2H$_2$O (Ln = Eu or Lu)**

|  | Eu | Lu |
| --- | --- | --- |
| formula | $C_{24}H_{36}EuF_6N_6O_6P$ | $C_{24}H_{36}F_6LuN_6O_6P$ |
| MW | 801.52 | 824.53 |
| cryst syst | orthorhombic | orthorhombic |
| no. | *Pbcn* | *Pbcn* |
| $T$/K | 100(2) | 100(2) |
| $a$/Å | 13.5742(6) | 13.5298(5) |
| $b$/Å | 15.9896(8) | 15.8653(7) |
| $c$/Å | 13.6143(6) | 13.5839(5) |
| $V$/Å$^3$ | 2954.9(2) | 2915.8(2) |
| $F(000)$ | 1608 | 1640 |
| $Z$ | 4 | 2 |
| $\lambda$, Å (MoK$_\alpha$) | 0.71073 | 0.71073 |
| $D_{calc}$/g cm$^{-3}$ | 1.802 | 1.878 |
| $\mu$/mm$^{-1}$ | 2.265 | 3.530 |
| $\theta$ range/deg | 9.49 to 27.49 | 9.52 to 26.38 |
| $R_{int}$ | 0.0649 | 0.0652 |
| reflns measd | 34134 | 31179 |
| unique reflns | 3245 | 2825 |
| reflns obsd | 2390 | 2065 |
| GOF on $F^2$ | 1.038 | 1.033 |
| $R1^a$ | 0.0224 | 0.0211 |
| $wR2$ (all data)$^b$ | 0.0486 | 0.0447 |
| Largest differences peak and hole/eÅ$^{-3}$ | 0.739 and −0.446 | 1.029 and −0.456 |

$^a R1 = \sum||F_0| - |F_c||/\sum|F_0|$. $^b wR2 = \{\sum[w(||F_0|^2 - |F_c|^2)^2]/\sum[w(F_0^4)]\}^{1/2}$.

**NMR Methods.** $^1H$ spectra of $[Tb(Me-DODPA)]Cl^{23}$ were recorded at 25 °C on a Bruker Avance 300 MHz spectrometer (300 MHz) by using a 30 mM solution of the complex in D$_2$O. *tert*-Butyl alcohol was used as an internal standard with the methyl signal calibrated at $\delta = 1.2$ ppm. $^1H$ NMR spectra of $[Tb(DOTAM)-(H_2O)]^{3+}$ were obtained at 25 °C on a JEOL EX90 spectrometer operating at 90 MHz for a 20 mM solution of the complex in D$_2$O (pD 7).

**Computational Methods.** All calculations presented in this work were performed employing the *Gaussian 09* package (Revision B.01).[32] Full geometry optimizations of the $[Gd(DOTA)(H_2O)]^-\cdot 2H_2O$, $[Gd(DOTAM)(H_2O)]^{3+}\cdot 2H_2O$, $[Gd(Py2N4Ac4)]^-$, $[Gd-(Py2N4Py4)]^{3+}$, and $[Gd(Me\text{-}DODPA)]^+$ systems were performed in aqueous solution employing DFT within the hybrid meta generalized gradient approximation (hybrid meta-GGA) with the TPSSh exchange-correlation functional.[33] We have shown previously that the TPSSh functional provides more accurate geometries of $Ln^{III}$ complexes than the popular B3LYP functional,[34] as well as accurate $^{17}O$ $A_{iso}$ values of the coordinated water molecule for different $Gd^{III}$ complexes with polyaminocarboxylate ligands.[22] On the grounds of our previous experience,[35] geometry optimizations were performed by using the large-core quasirelativistic effective core potential (LCECP) of Dolg and co. and its associated [5s4p3d]-GTO valence basis set,[36] whereas the ligand atoms were described by using the standard 6-31G(d,p) basis set. Input geometries of the $DOTA^{4-}$, Py2N4Py4, and Me-DODPA$^{2-}$ complexes were taken from previous computational studies.[23,25,37] For the $[Gd(Py2N4Ac4)]^-$ complex, the X-ray structure of the $Tb^{III}$ analogue was used as input structure.[24] The stationary points found on the potential energy surfaces as a result of the geometry optimizations have been tested to represent energy minima rather than saddle points via frequency analysis.

Two different approaches were used for the calculation of $^1H$ hyperfine coupling constants: (i) the small-core energy-consistent quasirelativistic effective core potential (SCECP) of Dolg and co.,[38] which includes 28 electrons in the core, in combination with the associated ECP28MWB_GUESS basis set,[39] and (ii) The all-electron second order Douglas-Kroll-Hess (DKH2) method as implemented in *Gaussian09*,[40] with the all-electron scalar relativistic basis set of Pantazis and Neese for Gd.[41] It has been shown that the calculation of hyperfine coupling constants with DFT requires the use of specifically developed basis sets with extra flexibility in the core region.[42] Thus, we used the EPR-III basis sets of Barone,[43] which were optimized for the computation of hyperfine coupling constants by DFT methods. EPR-III is a triple-ζ basis set including diffuse functions, double d-polarizations, a single set of f-polarization functions, and contains an improved s-part to better describe the nuclear region. The highest spin state was considered as the ground state (octuplet, $4f^7$) in all cases. Because the calculation of hyperfine coupling constants was performed by using an unrestricted model, spin contamination[44] was assessed by a comparison of the expected difference between $S(S + 1)$ for the assigned spin state ($S(S + 1) = 15.75$ for the mononuclear $Gd^{III}$ complexes investigated here) and the actual value of $\langle S^2 \rangle$.[45] The results obtained indicate that spin contamination is negligible for all systems investigated in this work. Convergence of the SCF procedure during the calculations of $^1H$ HFCCs was found to be problematic in some cases, and therefore a quadratically convergent SCF procedure was used when first order SCF did not achieve convergence (using the scf = xqc keyword in g09). The default values for the integration grid (75 radial shells and 302 angular points) and the SCF energy convergence criteria ($10^{-8}$) were used in all calculations. Geometry optimizations of the $[Gd(Py2N4Ac4)]^-$ system were also carried out by using the small-core approach as described above in combination with the 6-31G(d,p) basis set for C, H, N, and O [TPSSh/SCECP/6-31G(d,p)].

Throughout this work, solvent effects were included by using the polarizable continuum model (PCM), in which the solute cavity is built as an envelope of spheres centered on atoms or atomic groups with appropriate radii. In particular, we used the integral equation formalism (IEFPCM) variant as implemented in *Gaussian 09*.[46]

## RESULTS AND DISCUSSION

**Solid State and Solution Structure of [Ln(Me-DODPA)]$^+$ Complexes.** Solid state structures of metal complexes obtained from X-ray crystallography are often useful to understand the corresponding structures in solution, although in some cases solid state structures were found not to be representative of the solution-phase structures. Single crystals of formulas $[Ln(Me\text{-}DODPA)](PF_6)\cdot 2H_2O$ (Ln = Eu

or Lu) were obtained by addition of a $KPF_6$ excess to aqueous solutions of the complexes and subsequent evaporation of the solutions at room temperature. The structures of the two compounds are isomorphous, crystallize in the orthorhombic *Pbcn* space group, and the asymmetric units contain half $[Ln(Me\text{-}DODPA)]^+$ and $PF_6^-$ units and a water molecule. The two noncoordinating water molecules present in the crystal lattice are involved in hydrogen-bonding interaction with the oxygen atoms of carboxylate groups O(1) [Eu: O(1W)···O(1) 2.85(3) Å, H(11W)···O(1) 1.97(5) Å, O(1W)-H(11W)···O(1) 160(4)°; Lu: O(1W)···O(1) 2.838(4) Å, H(11W)···O(1) 2.05(6) Å, O(1W)-H(11W)···O(1) 164(5)°]. The [Ln(Me-DODPA)]$^+$ complexes possess a crystallographically imposed $C_2$ symmetry, where the symmetry axis is perpendicular to the leastsquares plane defined by the nitrogen atoms of the cyclen unit and contains the $Ln^{III}$ ion. Figure 1 shows a view of the
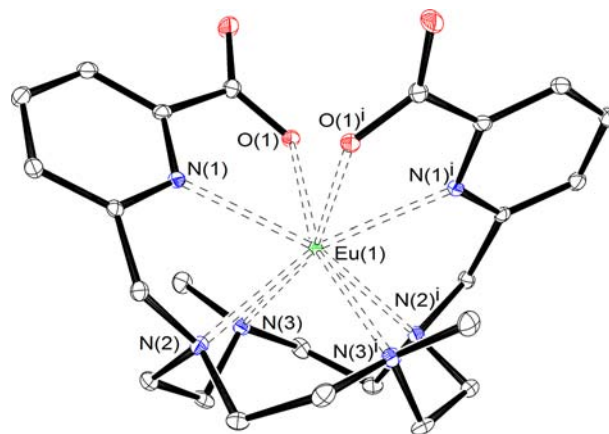


**Figure 1.** X-ray crystal structure of the cation [Eu(Me-DODPA)]$^+$ with atom labeling; hydrogen atoms are omitted for simplicity. The ORTEP plot is drawn at the 30% probability level.

**Table 2. Bond Lengths (Å) of the Metal Coordination Environments in [Ln(Me-DODPA)]$^+$ Complexes Obtained from X-ray Diffraction Analyses; See Figure 1 for Labeling**

|  | Eu | Lu |
|---|---|---|
| Ln(1)−O(1) | 2.325(2) | 2.236(2) |
| Ln(1)−N(1) | 2.471(2) | 2.380(2) |
| Ln(1)−N(2) | 2.595(2) | 2.517(3) |
| Ln(1)−N(3) | 2.593(2) | 2.522(2) |

[Eu(Me-DODPA)]$^+$ complex, whereas bond distances of the metal coordination environments are given in Table 2. As expected, the distances between the metal ions and the donor atoms of the ligand decrease along the lanthanide series from Eu to Lu as a consequence of the lanthanide contraction,[47] which also results in a slight decrease of the crystal cell parameters (Table 1). The metal ions are directly bound to the eight donor atoms of the ligand, which adopts a syn conformation with the two pendant arms disposed on the same side of the macrocyclic unit. The distances between the $Ln^{III}$ ion and the nitrogen atoms of the cyclen unit are ca. 0.12 Å longer than the Ln(1)−N(1) distances. The distances between the $Lu^{III}$ ion and the nitrogen atoms of the cyclen moiety are ca. 0.09 Å shorter than those observed for $[Lu(DOTA)]^-$ pointing to a rather strong binding of the cyclen unit to the metal ion.[48] As described in detail for $Ln^{III}$ complexes with cyclen-based ligands,[49] the syn conformation of

the ligand in [Ln(Me-DODPA)]⁺ complexes implies the occurrence of two helicities, one belonging to the crown moiety and one associated with the layout of the pendant arms.[50,51] Inspection of the crystal structure data reveals that two $\Delta(\delta\delta\delta\delta)$ and $\Lambda(\lambda\lambda\lambda\lambda)$ enantiomers cocrystallize in equal amounts (racemate).

The ¹H NMR spectrum of the paramagnetic Tb^III complex of Me-DODPA²⁻ was obtained in D₂O solution at pD 7.0 and 298 K (Figure 2, also Table 3). It shows 14 signals corresponding to
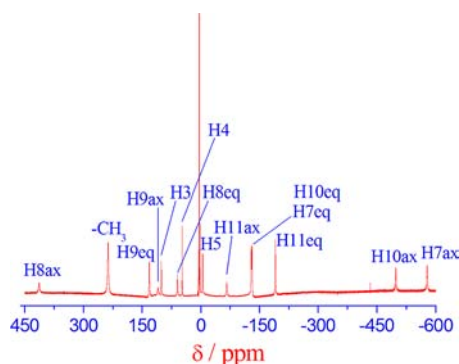


**Figure 2.** ¹H NMR spectrum of [Tb(Me-DODPA)]⁺ recorded in D₂O solution (pD ∼7.0) at 298 K. See Chart 1 for labeling.

14 magnetically nonequivalent proton environments in the ligand (Chart 1 for labeling). This points to an effective $C_2$ symmetry of the complex in solution suggesting that the metal coordination environment observed in the solid state for the Eu^III and Lu^III complexes is maintained in solution. The ten ¹H NMR signals due to protons of the cyclen unit can be grouped into two different sets according to their relative line broadening: five resonances with linewidths at half height of 540−990 Hz (at 300 MHz and 298 K), and five signals with linewidths in the range 305−420 Hz (Figure 2). These two sets of signals correspond to two sets of Tb^III−proton distances,

where the broader resonances are associated to axial protons and the sharper ones to equatorial protons.[52] The signals of the pyridyl protons are considerably sharper (120−270 Hz) as a consequence of the longer Tb···H distances for these nuclei. A full assignment of the ¹H NMR spectrum of [Tb(Me-DODPA)]⁺ was finally achieved by comparison to the shifts observed for the Yb^III analogue. Indeed, the paramagnetic shifts observed for these complexes roughly follow the Bleaney coefficients that govern the pseudocontact contributions,[9] and take values of 22 and −86 for Yb^III and Tb^III, respectively. Thus, the Tb^III complex is expected to provide paramagnetic shifts ca. 4 times larger than the Yb^III analogue and reversed in sign.

Prior calculation of its ¹H HFCCs, the [Gd(Me-DODPA)]⁺ complex was fully optimized in aqueous solution (IEFPCM model) at the TPSSh/LCECP/6-31G(d,p) level. The calculated bond distances of the metal coordination environment are the following: Gd(1)−O(1), 2.342 Å; Gd(1)−N(1), 2.557 Å; Gd(1)−N(2), 2.708 Å; Gd(1)−N(3), 2.684 Å. The calculated Gd(1)−O(1) distance is very similar to that observed in the solid state for the Eu^III complex (Table 1), whereas our calculations overestimate the Gd−N distances by 0.08−0.11 Å. Similar trends have been previously observed in DFT studies of different Ln^III complexes with cyclen-based ligands.[35] The optimized geometry of [Gd(Me-DODPA)]⁺ was used to compute ¹H HFCCs at the ligand nuclei with the aid of all-electron relativistic calculations based on the DKH2 method (DKH2/Neese/EPR-III). The ¹H HFCCs (Table 3) point to the presence of both positive and negative spin densities depending on the particular ligand nucleus, with $A_{iso}$ values ranging from −0.097 to 0.010 MHz.

For a given series of isostructural Ln^III complexes, the pseudocontact and contact shifts are proportional to the Bleaney constants and $\langle S_z \rangle$ (eq 2) respectively, which are characteristic of the particular Ln^III ion. The ratio of the Bleaney contants and $\langle S_z \rangle$ for the different paramagnetic Ln^III ions (except Gd^III) ranges from 1.89 for Eu^III to 0.12 to Yb^III.[9] Thus, the hyperfine ¹H NMR shifts in Yb^III complexes are

**Table 3.** ¹H NMR Shifts ($\delta_i^{obs}$, ppm), Observed Paramagnetic Shifts ($\delta_i^{para}$, ppm), Computed $A_{iso}$ Values (MHz), and Contact ($\delta_i^{con}$, ppm) and Pseudocontact ($\delta_i^{pscon}$) Contributions in [Tb(Me-DODPA)]⁺ at 298 K (Chart 1 for Labeling)

| | $\delta_i^{obs}$ | $\delta_i^{para}$ | $\delta_{i,calcd}^{para\ a}$ | $A_{iso}^{\ b}$ | $\delta_i^{con\ c}$ | $\delta_i^{pscon}$ | $\delta_{i,calcd}^{pscon\ a}$ |
|---|---|---|---|---|---|---|---|
| H3 | 101.2 | 93.2 | 97.2 | 0.00205 | 1.2 | 92.0 | 99.2 |
| H4 | 47.9 | 39.7 | 37.1 | −0.01015 | −5.7 | 45.4 | 39.9 |
| H5 | −4.6 | −12.4 | −18.0 | −0.01368 | 7.7 | −4.7 | −12.7 |
| H7ax | −578.2 | −582.5 | −587.5 | 0.00998 | 5.6 | −588.1 | −578.8 |
| H7eq | −129.1 | −133.8 | −121.7 | −0.06536 | −36.7 | −97.1 | −112.4 |
| H8ax | 412.9 | 410.2 | 426.3 | −0.00122 | −0.7 | 410.9 | 433.5 |
| H8eq | 60.0 | 57.0 | 94.7 | −0.08759 | −49.2 | 106.2 | 101.3 |
| H9ax | 109.8 | 106.7 | 99.5 | 0.00529 | 3.0 | 103.7 | 105.2 |
| H9eq | 132.0 | 129.3 | 157.2 | −0.04732 | −26.6 | 155.9 | 155.3 |
| H10ax | −498.0 | −501.3 | −483.7 | 0.00446 | 2.5 | −503.8 | −497.2 |
| H10eq | −130.8 | −133.9 | −100.5 | −0.03386 | −19.2 | −114.9 | −105.7 |
| H11ax | −66.4 | −69.7 | −70.57 | 0.00079 | 0.4 | −70.1 | −62.8 |
| H11eq | −190.7 | −193.69 | −169.0 | −0.03459 | −19.43 | −174.3 | −164.6 |
| $\chi_{zz} - \frac{1}{3}Tr\chi^{\ d}$ | | | 760 ± 313 | | | | 990 ± 162 |
| $\chi_{xx}\chi_{yy}^{\ d}$ | | | −33048 ± 554 | | | | −32950 ± 284 |
| AF$_j^{\ e}$ | | | 0.0737 | | | | 0.0381 |

$^a$Calculated values were obtained using eq 3 and the $\Lambda(\lambda\lambda\lambda\lambda)$ form of the complex optimized in aqueous solution at the TPSSh/LCECP/6-31G(d,p) level. $^b A_{iso}$ values calculated for the Gd^III analogue at the TPSSh/DKH2/Neese/EPR-III level. Calculated $A_{iso}$ values were averaged over symmetry equivalent nuclei. $^c$Obtained from the $A_{iso}$ values calculated for the Gd^III analogue with eq 2. $^d$Estimated using eq 3. $^e$AF$_j = [\sum_i (\delta_i^{exp} - \delta_i^{cal})/\sum_i (\delta_i^{exp})^2]^{1/2}$, where $\delta_i^{exp}$ and $\delta_i^{exp}$ represent the experimental and calculated values of a nucleus $i$, respectively.

**Table 4. Computed Hyperfine Coupling Constants ($A_{iso}$, MHz) for $[Gd(DOTA)(H_2O)]^- \cdot 2H_2O$ and $[Gd(DOTAM)(H_2O)]^{3+} \cdot 2H_2O$ Complexes (TPSSh).[a]**

| ligand | isomer | method | H1ax | H1eq | H2ax | H2eq | H3ax | H3eq |
|--------|--------|--------|------|------|------|------|------|------|
| DOTA$^{4-}$ | SAP | SCECP | 0.00199 | −0.06213 | −0.00608 | −0.08738 | −0.00075 | −0.08017 |
| | | DKH2 | 0.00218 | −0.06098 | −0.00598 | −0.08677 | 0.00027 | −0.07590 |
| DOTA$^{4-}$ | TSAP | SCECP | 0.00097 | −0.06310 | −0.00161 | −0.08105 | 0.01070 | −0.02830 |
| | | DKH2 | 0.00120 | −0.06580 | −0.00250 | −0.08370 | 0.01330 | −0.02640 |
| DOTAM | SAP | SCECP | 0.00350 | −0.06330 | −0.00598 | −0.09745 | 0.00171 | −0.09604 |
| | | DKH2 | 0.00372 | −0.06280 | −0.00590 | −0.09811 | 0.00275 | −0.09321 |

[a]Chart 1 for labeling. Calculated $A_{iso}$ values were averaged over symmetry equivalent nuclei.

largely dipolar in origin, and therefore they have been successfully analyzed by using eq 3. This ratio takes a value of 0.37 for Tb$^{III}$, and thus contact contributions may be responsible for a non-negligible part of the overall $^1$H paramagnetic shifts observed for these complexes. To test the accuracy of the $A_{iso}$ values calculated for $[Gd(Me\text{-}DODPA)]^+$, we have initially analyzed the experimental Tb$^{III}$-induced paramagnetic shifts by assuming that they are dominated by psedocontact contributions as given by eq 3. A least-squares fit to eq 3 was performed by using the Cartesian coordinates taken from the optimized geometries of the Gd$^{III}$ complex. The molecule was oriented so that its pseudo $C_2$ symmetry axis coincides with the Cartesian z axis,[53] whereas the orientation of the magnetic axis in the xy plane was allowed to vary during the least-squares procedure. A reasonable agreement between the experimental and calculated $\delta_i^{para}$ values was obtained according to the dipolar model, with an agreement factor $AF_j = 0.074$ (Table 3). However, relatively large deviations are observed for protons H8eq, H9eq, H10eq, and H11eq suggesting relatively important contact contributions for these proton nuclei. Interestingly, these proton nuclei correspond to those with largest calculated $A_{iso}$ values. Thus, the contact contributions for the different proton nuclei in $[Gd(Me\text{-}DODPA)]^+$ were obtained from the $A_{iso}$ values calculated for the Gd$^{III}$ analogue (Table 3) with the use of eq 2 and $\langle S_z \rangle = 31.853$.[9] The contact shifts obtained in this way for each proton nucleus were subtracted from the observed paramagnetic shift (Table 3), thereby providing the corresponding pseudocontact shifts, which were analyzed again by using eq 3 as described above. An important improvement of the agreement between experimental and calculated paramagnetic shifts is observed upon consideration of the contact shifts, as judged by the decrease of the agreement factor $AF_j$ from 0.074 to 0.038. These results indicate that the calculated geometry of $[Gd(Me\text{-}DODPA)]^+$ represents a good model for the structure of this complex in solution, and suggest that the contact contributions obtained for the Tb$^{III}$ complex on the basis of $A_{iso}$ values calculated for the Gd$^{III}$ analogue are reasonably accurate. As expected for a nonaxial system, the calculated $(\chi_{zz} - \frac{1}{3}Tr\chi)$ and $\chi_{xx} - \chi_{yy}$ values define a rhombic magnetic susceptibility tensor.

**Tb$^{III}$–Induced Paramagnetic Shifts in Other Macrocyclic Complexes.** Aiming to check if the methodology applied in the previous section might be of general applicability for rigid Tb$^{III}$ complexes, we have analyzed the paramagnetic shifts induced by this ion in different complexes with macrocyclic ligands. In a recent article, we have reported the molecular geometries of the SAP and TSAP isomers of $[Gd(DOTA)(H_2O)]^- \cdot 2H_2O$ complexes optimized in aqueous solution (IEFPCM model) at the TPSSh/LCRECP/6-31G(d) level.[22] In this work, we have used these previously reported structures to calculate isotropic $^1$H hyperfine coupling

constants. For $[Gd(DOTAM)(H_2O)]^{3+} \cdot 2H_2O$, the molecular geometry of the SAP isomer was fully optimized at the same computational level prior calculation of the $^1$H $A_{iso}$ values at the ligand nuclei. The explicit inclusion of two second-sphere water molecules has been proven to be crucial to obtain accurate distances between Gd$^{III}$ and the oxygen atom of the coordinated water molecule and $^{17}$O HFCCs.[22] The calculated average Gd−N and Gd−O$_{amide}$ distances in $[Gd(DOTAM)(H_2O)]^{3+} \cdot 2H_2O$ (2.687 and 2.453 Å, respectively) are in reasonably good agreement with those observed in the solid state (ca. 2.65 and 2.38 Å), whereas the calculated Gd−O$_{water}$ distance (2.39 Å) is very similar to those observed in the solid state for $[Gd(DOTAM)(H_2O)](CF_3SO_3)_3 \cdot 3H_2O$ (2.39 Å) and $[Gd(DOTAM)(H_2O)](NO_3)_3$ (2.35 Å).[54]

$^1$H HFCCs at the ligand nuclei in DOTA$^{4-}$ and DOTAM complexes with Gd$^{III}$ were calculated by using two different approaches: The effective core potential method for Gd in combination with the EPR-III basis set for the ligand atoms (SCECP/EPR-III), and all-electron relativistic calculations based on the DKH2 method (DKH2/Neese/EPR-III). The results reported in Table 4 indicate that the DKH2 and SCECP approaches give $^1$H $A_{iso}$ values in good mutual agreement, with differences typically lower than $4 \times 10^{-3}$ MHz. It must be pointed out that our SCECP/EPR-III calculations used point charges for the nuclei, whereas DKH2 calculations employed a Gaussian nuclear model. The good agreement obtained between SCECP and DKH2 calculations in the present investigation indicates that point charge model approximation can be safely used to calculate $^1$H HFCCs at the ligand nuclei of Gd$^{III}$ complexes. The $^1$H $A_{iso}$ values calculated for the different proton nuclei are substantially different: equatorial proton nuclei present negative $A_{iso}$ values ranging from −0.026 to −0.098 MHz, whereas axial proton nuclei give smaller absolute values for $A_{iso}$, which may have both positive and negative spin densities, and ranging from ca. +0.013 to −0.006 MHz. In a previous work, we have shown that $^{17}$O HFCCs of coordinated water molecules are very sensitive to the presence of second-sphere water molecules. However, calculations performed on the $[Gd(DOTA)(H_2O)]^-$ system at the DKH2/Neese/EPR-III level provide $^1$H HFCCs that deviate from those reported in Table 4 by $8 \times 10^{-5}$ to $6 \times 10^{-3}$ MHz, which shows that the inclusion of second sphere water molecules has a minor impact on the $^1$H HFCCs at the ligand nuclei.

Different computational studies on lanthanide complexes have shown that geometry optimizations using 4f-in-core calculations provide longer metal−donor distances than the corresponding small-core calculations.[55] Thus, we performed geometry optimizations of the $[Gd(Py2N4Ac4)]^-$ system by using both the large-core and small-core approaches to evaluate the effect of complex geometry on the calculated $A_{iso}$ values.

13424

dx.doi.org/10.1021/ic302322r | *Inorg. Chem.* 2012, 51, 13419−13429

Both approaches provide optimized geometries with nearly undistorted $D_2$ symmetries, as observed for the X-ray structures. Large-core calculations provide Gd–N$_{pyridine}$ and Gd–N$_{amine}$ distances (2.631 and 2.685 Å, respectively) being only slightly longer than those obtained from small-core computations (respectively 2.620 and 2.660 Å). However, Gd–O distances obtained from small-core calculations (2.414 Å) are considerably shorter than the large-core counterparts (2.475 Å). Table 5 presents the $A_{iso}$ values obtained for [Gd-

### Table 5. Computed Hyperfine Coupling Constants ($A_{iso}$, MHz) for [Gd(Py2N4Ac4)]$^-$ Complexes (TPSSh)$^a$

|      | SCECP (LC)$^b$ | SCECP (SC)$^c$ | DKH2(LC)$^b$ | DKH2(SC)$^c$ |
|------|---------------|---------------|-------------|-------------|
| H1   | −0.00466      | −0.00463      | −0.00577    | −0.00578    |
| H2   | −0.00518      | −0.00466      | −0.00405    | −0.00299    |
| H3ax | 0.00831       | 0.00749       | 0.00879     | 0.00842     |
| H3eq | −0.05143      | −0.05250      | −0.05323    | −0.05206    |
| H4ax | −0.00180      | −0.00227      | −0.00216    | −0.00271    |
| H4eq | −0.08412      | −0.08394      | −0.08533    | −0.08370    |
| H5ax | 0.01744       | 0.01925       | 0.01965     | 0.02266     |
| H5eq | −0.02161      | −0.01922      | −0.01587    | −0.01073    |

$^a$Calculated $A_{iso}$ values were averaged over symmetry equivalent nuclei. $^b$Values computed on the basis of the complex geometry optimized with LCECP calculations. $^c$Calculated using the complex geometry optimized with SCECP calculations.

(Py2N4Ac4)]$^-$ at the TPSSh/SCECP/EPR-III and TPSSh/DKH2/Neese/EPR-III levels on the basis of geometries obtained with large-core and small-core approaches. Our results show that computations based on LCECP and SCECP optimized geometries provide very similar $A_{iso}$ values. This also holds for H5ax and H5eq, which are at a four-bond distance of the Gd$^{III}$ ion through the Gd–O bonds. Thus, we conclude that the use of LC- or SC-optimized geometries for the calculation of $^1$H HFCCs does not affect substantially the computed vales. The data shown in Table 5 also confirm that

the SCECP and DKH2 approaches give very similar results. As observed for the DOTA$^{4-}$ and DOTAM complexes the equatorial protons present negative $A_{iso}$ values, while both positive and negative HFCCs are calculated for axial proton nuclei. The absolute $A_{iso}$ values are smaller for axial protons than for equatorial ones. The $^1$H HFCCs calculated for the CH$_2$ proton nuclei of [Gd(Py2N4Py4)]$^{3+}$ at the TPSSh/DKH2 level show a similar trend (Table S1 of the Supporting Information). The proton nuclei of the pyridyl units H1 and H2 present relatively small negative spin densities. The $A_{iso}$ values calculated for protons H6–H9 in [Gd(Py2N4Py4)]$^{3+}$ are also negative, with values ranging from −0.0073 MHz for H7 to −0.0425 MHz for H9.

The $^1$H NMR spectra of different [Ln(DOTAM)]$^{3+}$ complexes have been reported in the literature (Ln = Eu,[56] Yb[57]). The $^1$H NMR spectrum of the Tb$^{III}$ analogue, which has never been reported, presents six different signals that can be grouped in two sets according to their linewidths at half height: three broad signals due to the axial protons, and three sharper signals attributable to the equatorial protons (Table 6).[58] A comparison of the $^1$H NMR chemical shifts for DOTA$^{4-}$ and DOTAM complexes indicates that the [Tb(DOTAM)]$^{3+}$ complex adopts SAP coordination in aqueous solution. To analyze the Tb$^{III}$-induced shifts in [Tb(DOTA)(H$_2$O)]$^-$ and [Tb(DOTAM)]$^{3+}$ the complexes were oriented so that the pseudo $C_4$ symmetry axis coincides with the Cartesian $z$ axis. With this orientation, $\chi_{xy}$, $\chi_{xz}$, and $\chi_{yz}$ are expected to be zero, as well as the $\chi_{xx} - \chi_{yy}$ term due to the axial symmetry of the complexes (eq 3). Therefore, only one parameter ($\chi_{zz} - \frac{1}{3}Tr\chi$) has to be included in the least-squares fit of the experimental data. The differences between the experimental and fitted Tb$^{III}$-induced paramagnetic shifts ($\Delta\delta$) for the two isomers of [Tb(DOTA)(H$_2$O)]$^-$ are shown in Figure 3 and Table 6. A reasonable agreement between the experimental and calculated values was obtained for the axial protons of the ligand in both isomers, whereas larger deviations are observed for H2eq and H3eq in the SAP isomer, and H1eq and H2eq for

### Table 6. Observed $^1$H NMR Paramangnetic Shifts ($\delta_i^{para}$, ppm), Contact ($\delta_i^{con}$, ppm) and Pseudocontact ($\delta_i^{pscon}$) Contributions for [Tb(DOTA)(H$_2$O)]$^-$ and [Tb(DOTAM)(H$_2$O)]$^{3+}$ (Chart 1 for Labeling)

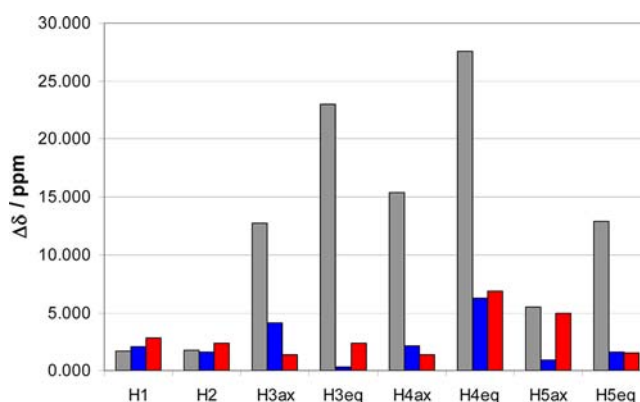| DOTA$^{4-}$ |      | H1ax   | H1eq  | H2ax  | H2eq   | H3ax  | H3eq  | $\chi_{zz} - \frac{1}{3}Tr\chi^c$ | AF$_j^d$ |
|-------------|------|--------|-------|-------|--------|-------|-------|-----------------------------------|----------|
| $\delta_i^{para\,a}$ | SAP  | −405.4 | −98.8 | 134.6 | −102.4 | 256.0 | 79.4  |                     |         |
|             | TSAP | −243.7 | −75.3 | 80.2  | −75.9  | 176.5 | 61.5  |                     |         |
| $\delta_{i,calcd}^{para}$ | SAP  | −392.6 | −79.4 | 132.0 | −64.4  | 270.4 | 108.3 | −13953 ± 411        | 0.1051  |
|             | TSAP | −250.6 | −50.7 | 84.1  | −41.2  | 172.8 | 69.1  | −8899 ± 290         | 0.1316  |
| $\delta_i^{con\,b}$ | SAP  | 1.2    | −34.8 | −3.4  | −49.6  | 0.2   | −43.4 |                     |         |
|             | TSAP | 0.7    | −37.6 | −1.4  | −47.8  | 7.6   | −15.1 |                     |         |
| $\delta_i^{pscon}$ | SAP  | −406.6 | −64.0 | 138.0 | −52.8  | 255.9 | 122.8 |                     |         |
|             | TSAP | −244.4 | −37.7 | 81.6  | −28.1  | 168.9 | 76.6  |                     |         |
| $\delta_{i,calcd}^{pscon}$ | SAP  | −392.1 | −79.3 | 131.8 | −64.4  | 270.0 | 108.3 | −13934 ± 325        | 0.0614  |
|             | TSAP | −241.8 | −48.9 | 81.2  | −39.7  | 166.7 | 66.7  | −8586 ± 183         | 0.0600  |
| **DOTAM**   |      |        |       |       |        |       |       |                     |         |
| $\delta_i^{para\,e}$ | SAP  | −319.4 | −85.6 | 105.7 | −81.0  | 202.1 | 56.0  |                     |         |
| $\delta_{i,calcd}^{para}$ | SAP  | −311.1 | −58.4 | 105.4 | −49.8  | 216.8 | 85.0  | −10801 ± 297        | 0.1289  |
| $\delta_i^{con\,b}$ | SAP  | 2.08   | −35.1 | −3.3  | −54.8  | 1.5   | −52.0 |                     |         |
| $\delta_i^{pscon}$ | SAP  | −321.5 | −50.6 | 109.0 | −26.3  | 200.6 | 108.0 |                     |         |
| $\delta_{i,calcd}^{pscon}$ | SAP  | −311.8 | −58.5 | 105.6 | −49.9  | 217.2 | 85.2  | −10821 ± 221        | 0.0946  |

$^a$Paramagnetic shifts at 20 °C from ref 59. $^b$Obtained from the $A_{iso}$ values calculated for the Gd$^{III}$ analogue at the TPSSh/DKH2/Neese/EPR-III level and eq 2. $^c$Estimated using eq 3. $^d$AF$_j$ = $[\sum_i(\delta_i^{exp} - \delta_i^{cal})^2/\sum_i(\delta_i^{exp})^2]^{1/2}$, where $\delta_i^{exp}$ and $\delta_i^{exp}$ represent the experimental and calculated values of a nucleus $i$, respectively. $^e$Obtained from the observed chemical shifts assuming $\delta_i^{dia}$ = 2.5 ppm.
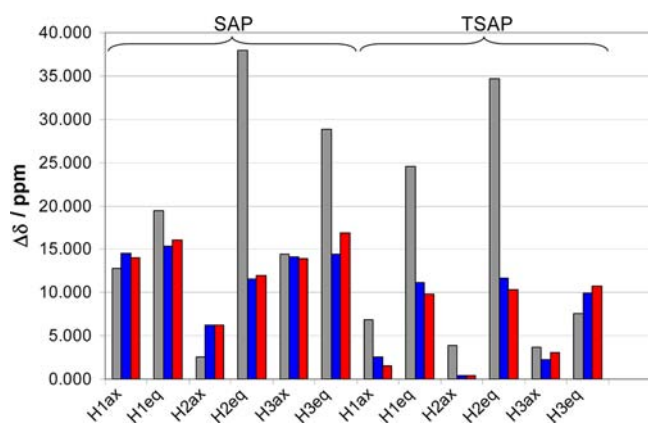
**Figure 3.** Absolute deviations ($\Delta\delta$) of experimental and calculated Tb$^{III}$-induced $^1$H NMR shifts in $[\text{Tb}(\text{DOTA})(\text{H}_2\text{O})]^-$. Gray, neglecting contact contributions; blue, contact contributions calculated at the TPSSh/RSC28/EPR-III level; red, contact contributions calculated at the TPSSh/DKH2/Neese/EPR-III level.



**Figure 4.** Absolute deviations ($\Delta\delta$) of experimental and calculated Tb$^{III}$-induced $^1$H NMR shifts in $[\text{Tb}(\text{Py2N4Ac4})]^-$. Gray, neglecting contact contributions; blue, contact contributions calculated at the TPSSh/RSC28/EPR-III level using the geometry of the complex optimized with the LC approach; red, contact contributions calculated at the TPSSh/RSC28/EPR-III level using the geometry of the complex optimized with the SC approach.

the TSAP form. Subsequently, the contact contributions for the different proton nuclei in $[\text{Tb}(\text{DOTA})(\text{H}_2\text{O})]^-$ were obtained from the $A_{iso}$ values calculated for the Gd$^{III}$ analogue (Table 4). An important diminution of the $\Delta\delta$ values is observed upon consideration of the contact shifts, particularly in the case of the ligand equatorial protons (Figure 3). As expected because of the similar $A_{iso}$ values, very similar $\Delta\delta$ values are obtained when contact contributions are estimated using the SCECP and DKH2 approaches. A similar conclusion is reached upon analysis of the NMR data of $[\text{Tb}(\text{DOTAM})]^{3+}$ (Figure S1 of the Supporting Information), although the improvement of the agreement upon inclusion of contact shifts is somewhat lower.

Analysis of the Tb$^{III}$-induced $^1$H NMR shifts in $[\text{Tb-(Py2N4Ac4)}]^-$ neglecting contact contributions provides a rather poor agreement between experimental and calculated data ($AF_j = 0.186$, Table 7). However, inclusion of the contact shifts in the analysis results in a spectacular improvement of the agreement factor $AF_j$, which takes a value of 0.033 when contact shifts are obtained at the TPSSh/SCECP/EPR-III level on the molecular geometry optimized using the LC approach. The same analysis performed using the complex geometry optimized using SC calculations provides similar agreement (Figure 4), which confirms that the use of LC or SC approaches for geometry optimization does not have an important impact in the global analysis. The better agreement observed for $[\text{Tb}(\text{Py2N4Ac4})]^-$ in comparison to the DOTA and DOTAM analogues may be attributed, at least in part, to distortions of the DFT optimized geometries from the idealized

$C_4$ symmetry in the latter complexes as a result of the presence of an inner-sphere water molecule. Analysis of the Tb$^{III}$-induced shifts in $[\text{Tb}(\text{Py2N4Py4})]^{3+}$ leads to similar results (Table S1 and Figure S2, Supporting Information). Indeed, inclusion of contact shifts, obtained from TPSSh/DKH2/Neese/EPR-III calculations on the Gd$^{III}$ analogue, improves the agreement factor $AF_j$ from 0.1258 to 0.0581.

A previous analysis of the Ln$^{III}$-induced shifts in $[\text{Tb-(Py2N4Ac4)}]^-$ complexes, where the contact and pseudocontact contributions were separated with the Reilley method lead to the conclusion that the principal magnetic axes of the paramagnetic susceptibility tensor do not pass through any symmetry element of the complexes.[24] This is in contrast with Neumann's general principle,[53] which implies that one direction of the general quadric must be aligned with the $C_2$ symmetry axis in monoclinic systems. The analysis reported here for $[\text{Tb}(\text{Py2N4Ac4})]^-$ and $[\text{Tb}(\text{Py2N4Py4})]^{3+}$ complexes show however that the principal magnetic axes of the paramagnetic susceptibility tensor are coincident with the three $C_2$ symmetry axes of the molecule.

**Spin Density Distributions.** The spin density distribution in a given paramagnetic molecule denotes the difference between the contributions due to electrons with majority spin ($\alpha$) and minority spin ($\beta$), and is the result of two effects: (i) spin-delocalization, that is, the transmission of spin density through the bonds toward the observed nucleus; (ii) spin-polarization, which is the result of an effective attraction of

**Table 7. Observed Paramangnetic Shifts ($\delta_i^{para}$, ppm), Contact ($\delta_i^{con}$, ppm), and Pseudocontact ($\delta_i^{pscon}$) Contributions for $[\text{Tb}(\text{Py2N4Ac4})]^-$ (Chart 1 for Labeling)**

| | H1 | H2 | H3ax | H3eq | H4ax | H4eq | H5ax | H5eq | $\chi_{zz} - \frac{1}{3}Tr\chi$ $^c$ | $\chi_{xx}$-$\chi_{yy}$ $^c$ | $AF_j$ $^d$ |
|---|---|---|---|---|---|---|---|---|---|---|---|
| $\delta_i^{para\,a}$ | −3.8 | 3.3 | 112.8 | 26.2 | 146.0 | 70.9 | −120.1 | −12.29 | | | |
| $\delta_{i,calcd}^{para}$ | −2.1 | 5.0 | 100.1 | 49.2 | 130.6 | 98.4 | −114.7 | 0.6 | 5105 ± 205 | −4523 ± 683 | 0.1864 |
| $\delta_i^{con\,b}$ | −2.6 | −2.9 | 4.7 | −28.9 | −1.0 | −47.3 | 9.8 | −12.1 | | | |
| $\delta_i^{pscon}$ | −1.2 | 6.2 | 108.1 | 55.1 | 147.0 | 118.1 | −129.9 | −0.1 | | | |
| $\delta_{i,calcd}^{pscon}$ | −3.3 | 4.6 | 112.2 | 54.8 | 149.1 | 111.9 | −129.0 | 1.5 | 5804 ± 39 | −4910 ± 131 | 0.0325 |

$^a$Paramagnetic shifts at 25 °C from ref 24. $^b$Obtained from the $A_{iso}$ values calculated for the Gd$^{III}$ analogue at the TPSSh/SCECP/EPR-III level and eq 2, on the molecular geometry optimized using the LC approach. $^c$Estimated using eq 3. $^d$$AF_j = [\sum_i(\delta_i^{exp} - \delta_i^{cal})^2/\sum_i(\delta_i^{exp})^2]^{1/2}$, where $\delta_i^{exp}$ and $\delta_i^{exp}$ represent the experimental and calculated values of a nucleus $i$, respectively.

unpaired electrons to the nearby ones of the same spin.[60] For a given metal center with occupied $\alpha$ and unoccupied $\beta$ orbitals, spin-delocalization can be identified either with metal to ligand $\alpha$ spin density donation, or by donation of $\beta$ spin density from the ligands to the metal center.[61] Both mechanisms create an excess of $\alpha$ spin density at the ligand nuclei, and therefore spin-delocalization gives always a positive contribution to the spin density, in contrast to spin-polarization, which can lead to a positive or negative contribution. Spin-polarization may be viewed as a response of the self-consistent electronic structure to a spin-delocalization acting as an initial driving force.

Figure 5 shows spin density maps calculated for [Gd(Me-DODPA)]$^+$ at the TPSSh/DKH2/Neese/EPR-III level. As
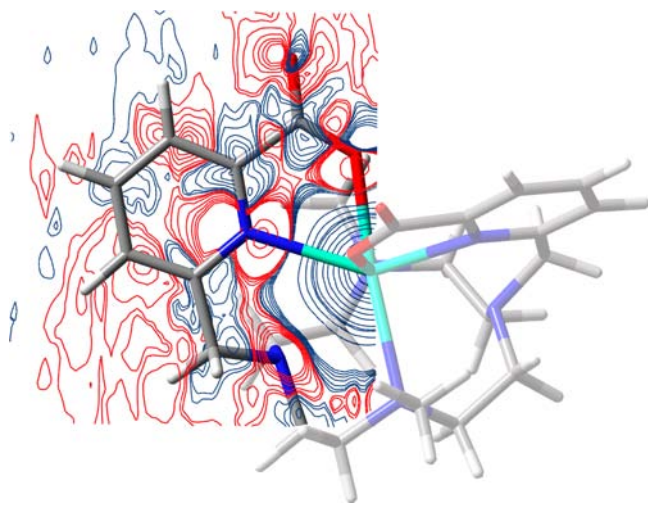


**Figure 5.** Contour spin density map obtained for the [Gd(Me-DODPA)]$^+$ system at the TPSSh/DKH2/Neese/EPR-III level on the plane defined by the Gd atom and the pyridyl unit. Positive spin densities are represented in blue and negative values in red.

found previously for [Gd(H$_2$O)$_8$]$^{3+}$ and [Gd(DTPA)-(H$_2$O)]$^{2-}$,[22,62] most of the positive spin density is placed on the Gd$^{III}$ ion itself, whereas the ligand donor atoms present negative spin densities indicating that spin-polarization effects dominate the $A_{iso}$ values for these nuclei. The spin-delocalization mechanism is expected to drop quickly as the number of bonds between the observed nuclei and the metal ion increases. Thus, if the spin-polarization mechanism dominates the contact shifts at the $^{14}$N and $^{17}$O nuclei of ligand donor atoms, most likely the same mechanism is also responsible for the $^1$H contact shifts observed at the ligand nuclei. A characteristic pattern pointing to a spin-polarization effect is the presence of alternate spin density (shift) signs along the pathway of the bonded atoms radiating out from the paramagnetic atom.[63] Figure 5 shows that this is indeed the case for the [Gd(Me-DODPA)]$^+$ system, where positive and negative spin densities are alternated along the carbon nuclei of the pyridyl units, and the Gd−N−C−H$_{eq}$ units of the macrocyclic fragment.

The spin density maps shown in Figure 5 indicate that most of the spin density is along the Gd−D bonds, where D represents a ligand donor atom. As a result, the spin density at proton nuclei in a Gd−D−C−H moiety is expected to depend on the dihedral angle between the Gd−D−C and D−C−H planes.[60] The very different $A_{iso}$ values calculated for axial and equatorial proton nuclei for the complexes investigated in this

work also point in this direction. Indeed, the Gd−D−C−H dihedral angles for equatorial proton nuclei take values in the range 160−180°, whereas axial protons give dihedral angles of about 70−80°. To investigate the effect of the Gd−D−C−H dihedral on the corresponding $^1$H $A_{iso}$ values we performed a relaxed potential energy surface scan of the [Gd(DOTA)-(H$_2$O)]$^-$·2H$_2$O system (SAP isomer) by changing the Gd−N−C−H2eq dihedral while keeping constant the Gd−N distance (Figure 6). Our results confirm the dependence of the $A_{iso}$ with
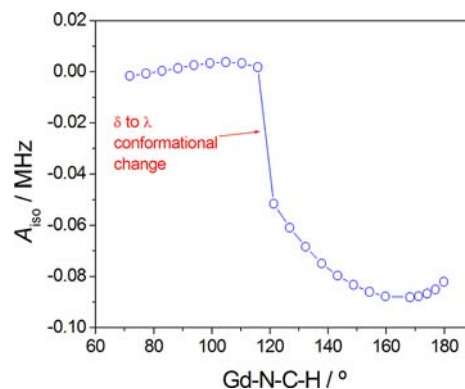


**Figure 6.** Dependence of the $^1$H $A_{iso}$ values with the Gd−N−C−H2eq dihedral angle in [Gd(DOTA)(H$_2$O)]$^-$·2H$_2$O (SAP isomer) as calculated at the TPSSh/DKH2/Neese/EPR-III level. The different geometries were obtained from a relaxed potential surface scan with the Gd−N distance fixed at 2.698 Å.

the Gd−D−C−H dihedral angle, in a similar way that the well-known empirical Karplus equation,[64] which describes the dependence of three-bond spin−spin coupling constants on the dihedral angle formed by the intervening single bonds. A similar angular dependence has been previously observed for spin−orbit-induced heavy-atom effects on NMR chemical shifts.[65]

The data shown in Figure 6 point to a relatively smooth change of $A_{iso}$ for Gd−D−C−H dihedrals in the range 120−180°. Decreasing the dihedral angle below 120° results in a sudden change of $A_{iso}$, which takes values close to zero for dihedral angles in the range 70−116°. This abrupt change in the calculated $A_{iso}$ values corresponds to a change in the conformation of the five-membered chelate ring from $\delta$ to $\lambda$, with a concomitant displacement of the proton from an equatorial to an axial position, and therefore a drop of its associated $A_{iso}$ value (above).

## ■ CONCLUSIONS

We have shown that the contact $^1$H NMR shifts at the ligand nuclei in Tb$^{III}$ complexes with macrocyclic ligands can be accurately calculated with DFT calculations performed on the Gd$^{III}$ analogues. Subsequent analysis of the pseudocontact shifts provided a very good agreement with the experiment, thereby validating the calculated contact shifts and the structures of the complexes in solution. The methodology reported herein represents an alternative to the classical Reilley method for the separation of the contact and pseudocontact shifts,[12,13a] which can be only applied for a series of isostructural lanthanide complexes under the assumption that the hyperfine coupling constant and crystal field parameters do not change significantly across the lanthanide series. Our approach can be classified in the context of model-dependent methods, which assume a

particular geometrical model (i.e., DFT optimized geometries) to perform the analysis of the paramagnetic shifts. However, we have shown previously that conformational analyses performed with the aid of DFT calculations provide accurate geometries of $Ln^{III}$ complexes in solution.[15b,66] Besides, the methodology reported here uses the paramagnetic shifts of a single $Ln^{III}$ ion ($Tb^{III}$), and therefore does not require to assume that pseudocontact shifts of different $Ln^{III}$ complexes of a given ligand are proportional to the Bleaney constants, which were derived with the assumption that the ligand field splittings for the lowest $J$ state are small compared to $kT$. It has been shown that the latter condition does not often hold in real lanthanide complexes.[67]

Spin-polarization effects appear to dominate the $^1H$ contact shifts investigated in this work, as indicated by the spin density distributions obtained from DFT calculations and the dependence of calculated $A_{iso}$ values on the Gd−N−C−H dihedral angle in $[Gd(DOTA)(H_2O)]^-$. This angular dependence of the $^1H$ HFCCs results in relatively important contact shifts for equatorial protons, while axial protons often present $A_{iso}$ values close to zero. The DKH2/Neese/EPR-III and RSC28/EPR-III approaches were shown to provide calculated HFCCs of essentially the same quality.

## ■ ASSOCIATED CONTENT

**ⓢ Supporting Information**

Absolute deviations ($\Delta\delta$) of experimental and calculated $Tb^{III}$-induced $^1H$ NMR shifts in $[Tb(Py2N4Py4)]^{3+}$ and $[Tb-(DOTAM)(H_2O)]^{3+}$ complexes, and optimized cartesian coordinates (Å) of the complexes investigated in this work. This material is available free of charge via the Internet at http://pubs.acs.org.

## ■ AUTHOR INFORMATION

**Corresponding Author**

*E-mail: carlos.platas.iglesias@udc.es.

**Notes**

The authors declare no competing financial interest.

## ■ ACKNOWLEDGMENTS

## ■ REFERENCES

(1) *The Chemistry of Contrast Agents in Medical Magnetic Resonance Imaging*; Merbach, A. E., Tóth, É., Eds.; Wiley: New York, 2001.

(2) (a) Caravan, P.; Ellinson, J. J.; McMurry, T. J.; Lauffer, R. B. *Chem. Rev.* **1999**, *99*, 2293−2352. (b) De Leon-Rodriguez, L. M.; Lubag, A. J. M.; Malloy, C. R.; Martinez, G. V.; Gillies, R. J.; Sherry, A. D. *Acc. Chem. Res.* **2009**, *42*, 948−957. (c) Aime, S.; Botta, M.; Terreno, E. *Adv. Inorg. Chem.* **2005**, *57*, 173−237. (d) Terreno, E.; Castelli, D. D.; Viale, A.; Aime, S. *Chem. Rev.* **2010**, *110*, 3019−3042.

(3) (a) Liu, S. *Adv. Drug Delivery Rev.* **2008**, *60*, 1347−1370. (b) Roesch, F. *Radiochim. Acta* **2007**, *95*, 303−311. (c) Volkert, W. A.; Hoffman, T. J. *Chem. Rev.* **1999**, *99*, 2269−2292. (d) Tweedle, M. F. *Acc. Chem. Res.* **2009**, *42*, 958−968.

(4) (a) Bünzli, J.-C. G. *Chem. Rev.* **2010**, *110*, 2729−2755. (b) Smith, D. G.; Pal, R.; Parker, D. *Chem.—Eur. J.* **2012**, *18*, 11604−11613. (c) Gabourdes, M.; Bourgine, V.; Mathis, G.; Bazin, H.; Alpha-Bazin, B. *Anal. Biochem.* **2004**, *333*, 105−113. (d) Lu, J.; Martin, J.; Lu, Y.;

Zhao, J.; Yuan, J.; Ostrowski, M.; Paulsen, I.; Piper, J. A.; Jin, D. *Anal. Chem.* **2012**, *84*, 9674−9678. (e) Zhang, H.; Tian, L.; Zhang, R.; Ye, Z.; Yuan, J. *Analyst* **2012**, *137*, 4502. (f) Lippert, A. R.; Gschneidtner, T.; Chang, C. J. *Chem. Commun.* **2010**, *46*, 7510−7512.

(5) (a) Ramasamy, R.; Castro, M. M. C. A.; de Freitas, D. M.; Geraldes, D. F. G. C. *Biochimie* **1992**, *74*, 777−783. (b) Weinstein, S. E.; Vining, M. S.; Wenzel, T. J. *Magn. Reson. Chem.* **1997**, *35*, 273−280. (c) Aspinall, H. C. *Chem. Rev.* **2002**, *102*, 1807−1850.

(6) (a) Rao, N. *J. Am. Chem. Soc.* **1988**, *110*, 8275−8287. (b) Allegrozzi, M.; Bertini, I.; Janik, M. B. L.; Lee, Y.-M.; Liu, G.; Luchinat, C. *J. Am. Chem. Soc.* **2000**, *122*, 4154−4161. (c) Barry, C. D.; North, A. C. T.; Glasel, J. A.; Williams, R. J. P.; Xavier, A. V. *Nature* **1971**, *232*, 236−245.

(7) (a) Pintacuda, G.; Otting, G. *J. Am. Chem. Soc.* **2002**, *124*, 372−373. (b) Bernini, A.; Spiga, O.; Venditti, V.; Prischi, F.; Botta, M.; Croce, G.; Pui-Ling Tong, A.; Wong, W.-T.; Niccolai, N. *J. Inorg. Biochem.* **2012**, *112*, 25−31.

(8) López-Vidal, E. M.; Regueiro-Figueroa, M.; Garcia, M. D.; Platas-Iglesias, C.; Peinador, C.; Quintela, J. M. *Inorg. Chem.* **2012**, *51*, 4429−4431.

(9) Peters, J. A.; Huskens, J.; Raber, D. J. *Prog. NMR Spectrosc.* **1996**, *28*, 283−350.

(10) Platas-Iglesias, C. *Eur. J. Inorg. Chem.* **2012**, 2023−2033.

(11) Viswanathan, S.; Kovacs, Z.; Green, K. N.; Ratnakar, S. J.; Sherry, A. D. *Chem. Rev.* **2010**, *110*, 2960−3018.

(12) (a) Di Pietro, S.; Lo Piano, S.; Di Bari, L. *Coord. Chem. Rev.* **2011**, *255*, 2810−2820. (b) Piguet, C.; Geraldes, C. F. G. C. Paramagnetic NMR lanthanide induced shifts for extracting solution structures. In *Handbook on the Physics and Chemistry of Rare Earths*; Bünzli, J.-C., Gschneidner, K. A., Eds.; Elsevier: North-Holland, 2003; Vol. 33, pp 353−463.

(13) (a) Reilley, C. N.; Good, B. W.; Desreux, J. F. *Anal. Chem.* **1975**, *47*, 2110−2116. (b) Kemple, M. D.; Ray, B. D.; Lipkowitz, K. B.; Prendergast, F. G.; Rao, B. N. D. *J. Am. Chem. Soc.* **1988**, *110*, 8275−8287. (c) Lisowski, J.; Sessler, J. L.; Lynch, V.; Mody, T. D. *J. Am. Chem. Soc.* **1995**, *117*, 2273−2285.

(14) Bleaney, B. *J. Magn. Reson.* **1972**, *8*, 91−100.

(15) (a) Mato-Iglesias, M.; Rodriguez-Blas, T.; Platas-Iglesias, C.; Starck, M.; Kadjane, P.; Ziessel, R.; Charbonnière, L. *Inorg. Chem.* **2009**, *48*, 1507−1518. (b) Mato-Iglesias, M.; Roca-Sabio, A.; Palinkas, Z.; Esteban-Gómez, D.; Platas-Iglesias, C.; Toth, E.; De Blas, A.; Rodriguez-Blas, T. *Inorg. Chem.* **2008**, *47*, 7840−7851.

(16) (a) Di Bari, L.; Pescitelli, G.; Sherry, A. D.; Woods, M. *Inorg. Chem.* **2005**, *44*, 8391−8398. (b) Vipond, J.; Woods, M.; Zhao, P.; Tircsó, G.; Ren, J.; Bott, S. G.; Ogrin, D.; Kiefer, G. E.; Kovacs, Z.; Sherry, A. D. *Inorg. Chem.* **2007**, *46*, 2584−2595.

(17) (a) Pinkerton, A. A.; Rossier, M.; Spiliadis, S. *J. Magn. Reson.* **1985**, *64*, 420−425. (b) Golding, R. M.; Pyykkö, P. *Mol. Phys.* **1973**, *26*, 1389−1396.

(18) Autschbach, J.; Pritchard, B. *Theor. Chem. Acc.* **2011**, *129*, 453−466.

(19) Autschbach, J.; Patchkovskii, S.; Pritchard, B. *J. Chem. Theory Comput.* **2011**, *7*, 2175−2188.

(20) (a) Barone, V.; Cimino, P.; Pedone, A. *Magn. Reson. Chem.* **2010**, *48*, S11−S22.

(21) (a) Saladino, A. C.; Larsen, S. C. *Cat. Today* **2005**, *105*, 122−133. (b) Schraut, J.; Arbuznikov, A. V.; Schinzel, S.; Kaupp, M. *ChemPhysChem* **2011**, *12*, 3170−3179.

(22) Esteban-Gomez, D.; de Blas, A.; Rodriguez-Blas, T.; Helm, L.; Platas-Iglesias, C. *ChemPhysChem* **2012**, *13*, 3640−3650.

(23) Rodriguez-Rodriguez, A.; Esteban-Gomez, D.; de Blas, A.; Rodriguez-Blas, T.; Fekete, M.; Botta, M.; Tripier, R.; Platas-Iglesias, C. *Inorg. Chem.* **2012**, *51*, 2509−2531.

(24) Valencia, L.; Martinez, J.; Macias, A.; Bastida, R.; Carvalho, R. A.; Geraldes, C. F. G. C. *Inorg. Chem.* **2002**, *41*, 5300−5312.

(25) Fernandez-Fernandez, M.; del, C.; Bastida, R.; Macias, A.; Perez-Lourido, P.; Platas-Iglesias, C.; Valencia, L. *Inorg. Chem.* **2006**, *45*, 4484−4496.

(26) Forsberg, J. H.; Delaney, R. M.; Zhao, Q.; Harakas, G.; Chandran, R. *Inorg. Chem.* **1995**, *34*, 3705−3715.

(27) Neese, F. *Coord. Chem. Rev.* **2009**, *253*, 526−563.

(28) Sheldrick, G. M. *SADABS Version 2.10*; University of Göttingen: Germany, 2004.

(29) SHELX Sheldrick, G. M. *Acta Crystallogr.* **2008**, *A64*, 112−122.

(30) Farrugia, L. J. *J. Appl. Crystallogr.* **1999**, *32*, 837−838.

(31) DIRDIF2008, Beurskens, P. T.; Beurskens, G.; de Gelder, R.; Garcia-Granda, S.; Gould, R. O.; Smits, J. M. M. *The DIRDIF2008 Program System, Crystallography Laboratory*; University of Nijmegen: The Netherlands, 2008.

(32) Frisch, M. J.; Trucks, G. W.; Schlegel, H. B.; Scuseria, G. E.; Robb, M. A.; Cheeseman, J. R.; Scalmani, G.; Barone, V.; Mennucci, B.; Petersson, G. A.; Nakatsuji, H.; Caricato, M.; Li, X.; Hratchian, H. P.; Izmaylov, A. F.; Bloino, J.; Zheng, G.; Sonnenberg, J. L.; Hada, M.; Ehara, M.; Toyota, K.; Fukuda, R.; Hasegawa, J.; Ishida, M.; Nakajima, T.; Honda, Y.; Kitao, O.; Nakai, H.; Vreven, T.; Montgomery, Jr., J. A.; Peralta, J. E.; Ogliaro, F.; Bearpark, M.; Heyd, J. J.; Brothers, E.; Kudin, K. N.; Staroverov, V. N.; Kobayashi, R.; Normand, J.; Raghavachari, K.; Rendell, A.; Burant, J. C.; Iyengar, S. S.; Tomasi, J.; Cossi, M.; Rega, N.; Millam, N. J.; Klene, M.; Knox, J. E.; Cross, J. B.; Bakken, V.; Adamo, C.; Jaramillo, J.; Gomperts, R.; Stratmann, R. E.; Yazyev, O.; Austin, A. J.; Cammi, R.; Pomelli, C.; Ochterski, J. W.; Martin, R. L.; Morokuma, K.; Zakrzewski, V. G.; Voth, G. A.; Salvador, P.; Dannenberg, J. J.; Dapprich, S.; Daniels, A. D.; Farkas, Ö.; Foresman, J. B.; Ortiz, J. V.; Cioslowski, J.; Fox, D. J. *Gaussian 09*, Rev. A.01; Gaussian, Inc.: Wallingford, CT, 2009.

(33) Tao, J. M.; Perdew, J. P.; Staroverov, V. N.; Scuseria, G. E. *Phys. Rev. Lett.* **2003**, *91*, 146401.

(34) Roca-Sabio, A.; Regueiro-Figueroa, M.; Esteban-Gomez, D.; de Blas, A.; Rodriguez-Blas, T.; Platas-Iglesias, C. *Comput. Theo. Chem.* **2012**, *999*, 93−104.

(35) Platas-Iglesias, C.; Roca-Sabio, A.; Regueiro-Figueroa, M.; Esteban-Gómez, D.; De Blas, A.; Rodríguez-Blas, T. *Curr. Inorg. Chem.* **2011**, *1*, 91−116.

(36) Dolg, M.; Stoll, H.; Savin, A.; Preuss, H. *Theor. Chim. Acta* **1989**, *75*, 173−194.

(37) Purgel, M.; Baranyai, Z.; de Blas, Z.; Rodríguez-Blas, T.; Banyai, I.; Platas-Iglesias, C.; Toth, I. *Inorg. Chem.* **2010**, *49*, 4370−4382.

(38) Dolg, M.; Stoll, H.; Preuss, H. *J. Chem. Phys.* **1989**, *90*, 1730−1734.

(39) Energy-consistent ECPs and associated basis sets are available at http://www.theochem.uni-stuttgart.de/index.en.html.

(40) (a) Barysz, M.; Sadlej, A. J. *J. Mol. Struct. (Theochem)* **2001**, *573*, 181−200. (b) Reiher, M. *Theor. Chem. Acc.* **2006**, *116*, 241−252.

(41) Pantazis, D. A.; Neese, F. *J. Chem. Theory Comput.* **2009**, *5*, 2229−2238.

(42) Orio, M.; Pantazis, D. A.; Neese, F. *Photosynth. Res.* **2009**, *102*, 443−453.

(43) Rega, N.; Cossi, M.; Barone, V. *J. Chem. Phys.* **1996**, *105*, 11060−11067.

(44) Stanton, J. F.; Gauss, J. *Adv. Chem. Phys.* **2003**, *125*, 101−146.

(45) Montoya, A.; Truong, T. N.; Sarofim, A. F. *J. Phys. Chem. A* **2000**, *124*, 6108−6110.

(46) Tomasi, J.; Mennucci, B.; Cammi, R. *Chem. Rev.* **2005**, *105*, 2999−3093.

(47) Seitz, M.; Oliver, A. G.; Raymond, K. N. *J. Am. Chem. Soc.* **2007**, *129*, 11153−11160.

(48) Aime, S.; Barge, A.; Botta, M.; Fasano, M.; Ayala, J. D.; Bombieri, G. *Inorg. Chim. Acta* **1996**, *246*, 423−429.

(49) Aime, S.; Botta, M.; Fasano, M.; Marques, M. P. M.; Geraldes, C. F. G. C.; Pubanz, D.; Merbach, A. E. *Inorg. Chem.* **1997**, *36*, 2059−2068.

(50) Corey, E. J.; Bailar, J. C., Jr. *J. Am. Chem. Soc.* **1959**, *81*, 2620−2629.

(51) Beattie, J. K. *Acc. Chem. Res.* **1971**, *4*, 253−259.

(52) Aime, S.; Barbero, L.; Botta, M.; Ermondi, G. *J. Chem. Soc., Dalton Trans.* **1992**, 225−228.

(53) Terazzi, E.; Rivera, J.-P.; Ouali, N.; Piguet, C. *Magn. Reson. Chem.* **2006**, *44*, 539−552.

(54) (a) Thompson, A. L.; Parker, D.; Fulton, D. A.; Howard, J. A. K.; Pandya, S. U.; Puschmann, H.; Senanayake, K.; Stenson, P. A.; Badari, A.; Botta, M.; Avedano, S.; Aime, S. *Dalton Trans.* **2006**, 5605−5616. (b) Bombieri, G.; Marchini, N.; Ciattini, S.; Mortillaro, A.; Aime, S. *Inorg. Chim. Acta* **2006**, *359*, 3405−3411.

(55) (a) Maron, L.; Eisestein, O. *J. Phys. Chem. A* **2000**, *104*, 7140−7143. (b) Guillaumont, D. *J. Phys. Chem. A* **2004**, *108*, 6893−6900.

(56) Aime, S.; Barge, A.; Bruce, J. I.; Botta, M.; Howard, J. A. K.; Moloney, J. M.; Parker, D.; de Sousa, A. S.; Woods, M. *J. Am. Chem. Soc.* **1999**, *121*, 5762−5771.

(57) Zhang, S.; Michaudet, L.; Burgess, S.; Sherry, A. D. *Angew. Chem., Int. Ed.* **2002**, *41*, 1919−1921.

(58) Aime, S.; Barbero, L.; Botta, M.; Ermondi, G. *J. Chem. Soc., Dalton Trans.* **1992**, 225−228.

(59) Marques, M. P. M.; Geraldes, C. F. G. C.; Sherry, A. D.; Merbach, A. E.; Powell, H.; Pubanz, D.; Aime, S.; Botta, M. *J. Alloys Compd.* **1995**, *225*, 303−307.

(60) Bertini, I.; Luchinat, C. *Coord. Chem. Rev.* **1996**, *150*, 29−75.

(61) (a) Aquino, F.; Pritchard, B.; Autschbach, J. *J. Chem. Theory Comput.* **2012**, *8*, 598−609. (b) Pritchard, B.; Autschbach, J. *Inorg. Chem.* **2012**, *51*, 8340−8351.

(62) Yazyev, O. V.; Helm, L.; Malkin, V. G.; Malkina, O. L. *J. Phys. Chem. A* **2005**, *109*, 10997−11005.

(63) Lisowski, J.; Sessler, J. L.; Mody, T. D. *Inorg. Chem.* **1995**, *34*, 4336−4342.

(64) (a) Karplus, M. *J. Am. Chem. Soc.* **1963**, *85*, 2870−2871. (b) Geraldes, C. F. G. C.; Sherry, A. D.; Kiefer, G. E. *J. Magn. Reson.* **1992**, *97*, 290−304.

(65) (a) Hegetschweiler, K.; Kuppert, D.; Huppert, J.; Straka, M.; Kaupp, M. *J. Am. Chem. Soc.* **2004**, *126*, 6728−6738. (b) Kaupp, M.; Malkina, O. L.; Malkin, V. G.; Pyykkö, P. *Chem.—Eur. J.* **1998**, *4*, 118−126.

(66) Roca-Sabio, A.; Mato-Iglesias, M.; Esteban-Gomez, D.; Toth, E.; de Blas, A.; Platas-Iglesias, C.; Rodriguez-Blas, T. *J. Am. Chem. Soc.* **2009**, *131*, 3331−3341.

(67) Mironov, V. S.; Galyametdinov, Y. G.; Ceulemans, A.; Gorller-Walrand, C.; Binnemans, K. *J. Chem. Phys.* **2002**, *116*, 4673−4685.